


PAPER

View Article Online
View Journal | View Issue

Cite this: *Biomater. Sci.*, 2024, **12**, 2418

3D printing nacre powder/sodium alginate scaffold loaded with PRF promotes bone tissue repair and regeneration†

Bin Liu,^{‡a,b} Cewen Hu,^{‡a} Xinyue Huang,^a Kaiqi Qin,^a Lei Wang,^a Zhilong Wang,^a Jiachen Liang,^a Fuqiang Xie^{*a,b} and Zengjie Fan  ^{*a}

Bone defects are a common complication of bone diseases, which often affect the quality of life and mental health of patients. The use of biomimetic bone scaffolds loaded with bioactive substances has become a focal point in the research on bone defect repair. In this study, composite scaffolds resembling bone tissue were created using nacre powder (NP) and sodium alginate (SA) through 3D printing. These scaffolds exhibit several physiological structural and mechanical characteristics of bone tissue, such as suitable porosity, an appropriate pore size, applicable degradation performance and satisfying the mechanical requirements of cancellous bone, etc. Then, platelet-rich fibrin (PRF), containing a mass of growth factors, was loaded on the NP/SA scaffolds. This was aimed to fully maximize the synergistic effect with NP, thereby accelerating bone tissue regeneration. Overall, this study marks the first instance of preparing a bionic bone structure scaffold containing NP by 3D printing technology, which is combined with PRF to further accelerate bone regeneration. These findings offer a new treatment strategy for bone tissue regeneration in clinical applications.

Received 28th November 2023,
Accepted 11th March 2024

DOI: 10.1039/d3bm01936e

rsc.li/biomaterials-science

1. Introduction

Bone defects are the most common complication of bone diseases, which are caused by trauma, tumours, inflammation, and developmental malformations.¹ They often significantly impact the quality of life of patients.² Clinically, small bone defects (with a diameter less than 6 mm) can be repaired by stimulating the potential of autologous bone regeneration, such as the natural healing of tooth extraction wounds;³ however, larger bone defects need to be repaired by surgical treatment. At present, the treatment methods for repairing bone tissue defects encompass methods such as autografts, allografts, xenografts, and the use of various bone graft materials.² Although the above treatment methods have shown certain clinical effects, there are many surgical complications (such as immune rejection, infection, and easy absorption of

implants)⁴ which limit the long-term clinical application of bone grafts.

In the 1990s, R. Langer and J. Vacant put forward the concept of “tissue engineering”. With the development of biotechnology, stem cell transplantation and cell cloning technology, the emergence of bone tissue engineering (BTE) provides a novel approach to address bone defect repair.^{2,5} BTE involves the transplantation of biodegradable scaffolds loaded with different kinds of cells and growth factors into bone defect sites to stimulate bone regeneration.⁶ The fundamental principle of BTE is to mimic the structure and function of the bone extracellular matrix (ECM). It aims to create a suitable three-dimensional environment that supports the proliferation of seed cells, directly facilitates osteogenic differentiation, and enables efficient delivery of nutrients.⁷ Natural biomacromolecule hydrogels, such as alginates, find extensive application in BTE due to their capacity to simulate the ECM.⁸ Among these, sodium alginate (SA), a natural anionic macromolecular polymer, is a significant material in BTE and bioprinting research. This is due to its low biotoxicity, biodegradability, and the ability to form a tightly crosslinked network structure through chemical crosslinking with divalent cations (such as Ca²⁺).⁹ However, SA hydrogel scaffolds have limitations, such as poor mechanical properties, excessive swelling, and a rapid degradation rate.¹⁰ These limitations may potentially hinder their osteogenic ability. To address this, nacre

^aKey Laboratory of Dental Maxillofacial Reconstruction and Biological Intelligence Manufacturing, Gansu Province, School of Stomatology, Lanzhou University, Lanzhou 730000, P. R. China. E-mail: zjfan@lzu.edu.cn

^bDepartment of Oral and Maxillofacial Surgery, 2nd Hospital of Lanzhou University, Lanzhou 730030, P. R. China. E-mail: lzu_xieff@lzu.edu.cn

†Electronic supplementary information (ESI) available. See DOI: <https://doi.org/10.1039/d3bm01936e>

‡These two authors contributed equally to this study.

powder (NP), a composite material derived from the innermost layer of animal shells, has emerged as a promising solution. NP resembles the structure of natural bone, comprising inorganic mineral phases and an organic matrix, predominantly aragonite calcium carbonate, constituting over 95% of its composition.^{11,12} NP exhibits excellent osteogenic activity in the bone healing process.¹³ Adding NP to SA hydrogel scaffolds has the potential to enhance their mechanical properties. Additionally, NP can regulate the degradation rate of SA hydrogel scaffolds to align with the rate of bone regeneration.¹⁴

The scaffold material also plays a crucial role in constructing the three-dimensional spatial structure of the ECM. Conventional methods for manufacturing BTE scaffolds mainly involve techniques such as electrospinning, freeze-drying, layer-by-layer self-assembly, *etc.*¹⁵ However, the processes of these methods are complicated, resulting in randomly irregular structures within the scaffolds. They lack the ability to precisely control the pore size and specific internal structures of the scaffolds,¹⁶ which limits their further progress in the field of BTE. In contrast, 3D printing has emerged as a promising scaffold fabrication technique. This innovative approach is characterized by its ability to accurately control the distribution of components and the structural morphology within the scaffolds, allowing for the construction of specific three-dimensional scaffold structures to some extent.¹⁷ This technology also promotes personalized control of pore size and porosity,^{18,19} which plays a crucial role in the mechanical and degradation properties of bone tissue scaffolds, as well as the formation of bionic vascularized bone. Wang *et al.* used 3D printing technology to fabricate a PCL scaffold with a dual-pore size gradient structure for bone-cartilage, demonstrating that the larger pore size scaffold (400 μm) located in the bone tissue layer is more beneficial for osteogenic differentiation and vascularization of BMSCs.²⁰ Feng *et al.* prepared personalized biomimetic materials with lotus root-like structures by 3D printing. This resulted in a significant improvement in the porosity and specific surface area of the biomimetic materials, leading to enhanced cell attachment and proliferation. Furthermore, these materials demonstrated proficiency in promoting osteogenesis and vascularization *in vivo*.²¹ Therefore, combining 3D printing technology with BTE holds immense potential in the development of personalized BTE scaffolds for the treatment of bone defects, offering a wide range of application prospects.²²

Bioactive substances can regulate and accelerate the process of bone regeneration. However, their clinical application is limited by factors such as high cost, susceptibility to inactivation, and certain immunogenicity.⁴ Platelet-rich fibrin (PRF) is a platelet concentration derived from venous blood, which is rich in host immune cells and growth factors,²³ such as platelets, white blood cells, vascular endothelial growth factor (VEGF), platelet-derived growth factor (PDGF), and transforming growth factor- β (TGF- β). These growth factors can be released from PRF, accelerating the process of angiogenesis to impact the remodelling of bone tissue.²⁴ PRF is widely used in oral clinical work, which can accelerate the healing of the

Table 1 Partial characterization value of NP/SA scaffolds

NP/SA (wt/wt)	0 : 1	1 : 2	1 : 1	2 : 1
Porosity (%)	73.74 \pm 5.81	63.38 \pm 2.71	58.51 \pm 3.68	51.38 \pm 4.06
Degradation rate (%)	39.56 \pm 0.79	25.97 \pm 0.84	21.94 \pm 0.85	31.63 \pm 0.80
Compression strength (MPa)	7.5 \pm 0.60	7.55 \pm 0.12	8.21 \pm 0.43	1.27 \pm 0.41
Compression modulus (MPa)	7.97 \pm 0.4	10.36 \pm 0.35	22.92 \pm 0.84	12.83 \pm 0.31

alveolar fossa and enhance the rate of bone regeneration.²⁵ Zhang *et al.* found that binding PRF to a multifunctional composite scaffold could release PDGF and TGF- β 1, thereby promoting bone formation.⁴ Additionally, Wang Z. *et al.* discovered that the combination of PRF and mesenchymal stem cells (MSCs) induces osteogenesis and formation of dense bone.²⁶ Therefore, PRF is an ideal bioactive material for BTE. It can be easily prepared from patients' venous blood, with a simple process that often requires only one step. It is highly cost-effective and possesses the ability to accelerate bone regeneration.²⁴ In a word, the combination of PRF and a composite scaffold can give full play to their excellent properties to induce osteogenic differentiation of bone marrow mesenchymal stem cells (BMSCs), providing an effective and feasible strategy for bone tissue repair and regeneration.

In this study, we utilized SA as the matrix material and incorporated NP in ratios of 0 : 1, 1 : 2, 1 : 1, and 2 : 1 to prepare printable bio-inks. NP/SA composite scaffolds were then fabricated using 3D printing technology. This innovative approach allows for the preparation of personalized and precise NP/SA composite bone scaffolds that closely match the bone defect area. We systematically evaluated the microstructure, porosity, degradation performance, and mechanical properties of the four scaffold groups. NP/SA (1 : 1) composite scaffolds were selected due to their closer alignment with the physiological structure of the trabecular bone and the mechanical properties of bone tissue (refer to Table 1). PRF, known for its richness in growth factors such as VEGF, PDGF, and TGF- β , was loaded into the NP/SA (1 : 1) scaffold group for subsequent *in vitro* and *in vivo* experiments to detect their osteogenic ability.

2. Materials and methods

2.1 Materials and chemical reagents

Nacre powder Pearl (NP, 500 mesh, 98%) was purchased from Aozhen Pharmaceutical Co., Ltd (Guangdong, China). SA (S278630, M_w = 222.0 kDa), CaCl_2 (C118445, M_w = 110.98 Da, 96%) and KBr (P433931, M_w = 119 Da, 99.4%) were purchased from Aladdin Biochemical Technology Co., Ltd (Shanghai, China). The osteogenic induction medium and alizarin red staining (ARS) solution were purchased from Gansu Ruiqi Biotechnology Co., Ltd (Lanzhou, China); penicillin-streptomycin, fetal bovine serum (FBS) and phosphate buffered saline (PBS) were purchased from HyClone Laboratories Inc. (UT, USA). Dimethyl sulfoxide (D103272, $\text{C}_2\text{H}_6\text{SO}$, M_w = 78.13 Da,

>99%) (DMSO) was purchased from Tianjin No. 1 Chemical Reagent Factory (Tianjin, China). Methyl thiazolyl tetrazolium bromide (MB4698, $C_{18}H_{16}BrN_5S$, MW = 414.32 Da, 98%) (MTT) and Calcein-AM/PI assay kit (C272922, $C_{46}H_{46}N_2O_{23}$, M_w = 994.86 Da, AM \geq 90%, PI \geq 95%) were purchased from Solarbio Science & Technology Co., Ltd (Beijing, China); ethyl carbamate ($C_3H_7NO_2$, M_w = 89.09 Da, 99%) was purchased from Runyou Chemical Co., Ltd (Shenzhen, China). Deionized water was prepared by laboratory pure water systems (Smart-S15, Hitech, Shanghai, China).

2.2 Preparation and characterization of NP/SA scaffolds

2.2.1 Preparation of NP/SA scaffolds by 3D printing. When the NP/SA scaffold was fabricated by 3D printing technology, 6% SA hydrogel solution was first prepared. Then, NP was added to the 6% SA hydrogel solution according to a certain proportion (NP:SA = 0:1, 1:2, 1:1 and 2:1, wt/wt) and stirred for 24 h to obtain a uniformly mixed NP/SA composite hydrogel. The series of composite hydrogel systems served as the bio-inks for 3D printing. The printability of the NP/SA bio-ink was evaluated using a stress-controlled rheometer (Anton-Paar, Austria). The viscosity of the bio-ink was measured across a shear rate range of 1 to 100 s^{-1} . In order to study the rheological behaviour of the bio-ink under oscillatory shear, the stress scanning test was conducted at a frequency of 1 Hz, and the values of storage modulus (G') and loss modulus (G'') were obtained. The prepared NP/SA bio-ink was printed layer by layer using a 3D bioprinter (Envision TEC Manufacture, Germany) with a total of 10 layers. The specific parameters were as follows: a dispensing needle with an inner diameter of 0.41 mm was selected, the extrusion pressure ranged from 1.4 to 1.8 bar, and the printing speed was set at 10 $mm s^{-1}$. After each layer was printed, the printed bio-ink was crosslinked using an electronic spray device containing $CaCl_2$ solution (100 mM) for several seconds to maintain the three-dimensional network structure of the scaffolds. Subsequently, the solidified NP/SA hydrogel composite scaffolds were thoroughly crosslinked with $CaCl_2$ solution for 10 min.²⁷ The scaffolds were washed three times with deionized water, pre-frozen at $-20^\circ C$ for 4 h, and freeze-dried at $-20^\circ C$ in a freeze dryer (Scientz-10n, China) for 48 h to obtain the final NP/SA composite scaffolds. Prior to subsequent experiments, they were respectively disinfected with ethanol (75%) and ultraviolet light and stored at $4^\circ C$.

2.2.2 Characterization of NP/SA scaffolds

NP/SA scaffold morphology. Scanning electron microscopy (SEM, JEOL JSM-6701F) was used to observe the surface morphology and pore size of the NP/SA scaffolds. The scaffolds were coated with gold at room temperature with a current of 10 mA, the ion sputtering time was 60 s. SEM images were captured at an operating voltage of 30 kV. To determine the average diameter of the pore size, NIH ImageJ software (v1.52e) was used to analyse three images of each sample at least.

Fourier transform infrared spectroscopy (FTIR). The functional groups and formed chemical bonds of the printed scaffolds were identified by FTIR (Bruker IFS66 V FTIR spectrometer).

To facilitate the analysis, the sample powder was prepared and fully mixed with pure potassium bromide (KBr), the sample powder/KBr (wt/wt) ratio was 1:100. Then the mixed powder was pressed into thin slices. By observing the infrared absorption peaks within the range of 400–4000 cm^{-1} with a resolution of 4 cm^{-1} , the wavelengths of these peaks were evaluated to determine the surface functional groups of NP/SA scaffolds. Each sample powder was measured at least three times.

X-ray diffraction (XRD) test. The XRD (Rigaku D/Max-2400) technique was used to analyse the phase of freeze-dried NP/SA scaffolds' powder. The prepared freeze-dried samples were ground into fine powder with a mortar, and the samples were kept dry before testing. The specific measurement conditions were as follows: the Bruker-AXS X-ray continuous spectrum scanning method was used to measure the voltage of 40 kV, the current of 40 mA, the radiation source of Cu-K α , the scanning range of 2θ from 5 to 80° , and the scanning rate was $10^\circ min^{-1}$.

Porosity evaluation. The porosity of NP/SA scaffolds could be evaluated according to the ethanol displacement method. The scaffolds were weighed, and their masses were then measured after being immersed in 100% ethanol for 48 h at room temperature. The porosity of the scaffolds was calculated using the following equation:⁴

$$\text{Porosity (\%)} = (W_2 - W_1) / (\rho(S \times h)).$$

Where W_2 is the weight of each scaffold immersed in ethanol, W_1 is the weight of each dry scaffold, ρ is the density of ethanol, S is the bottom area of each scaffold, and h is the height of each scaffold ($n \geq 3$).

Water contact angle measurement. The hydrophilicity of NP/SA scaffolds was examined using a contact angle measurement instrument (SZ-CAMB1, Sunzeru, China). When measuring the water contact angle, the volume of water droplets was 5 μL . Photos of water contact angles were captured with a colour CCD camera (SZ-CAMB1, Sunzeru, China), all samples were measured at least three times. The contact angles of all samples were calculated using Draw Tool (Microsoft, Richmond, WA) ($n \geq 3$).

Swelling rate test. The freeze-dried NP/SA scaffolds were weighed and recorded as W_3 . They were immersed in PBS (pH = 7.4) at $37^\circ C$ for 0.5, 1, 2, 4, 8, 12, and 24 h. The whole experiment was carried out in an incubator at $37^\circ C$. At each predetermined time point, the scaffolds (at least 3 samples in each group) were taken out from PBS solution, the excess liquid was removed with filter paper, the scaffolds were re-weighed and recorded as W_4 . The swelling ratio (SR) was calculated using the following equation:

$$\text{Swelling ratio (\%)} = (W_4 - W_3) / W_3 \times 100.$$

Where W_3 represents the initial dry weight of the samples and W_4 represents the weight of the samples after swelling ($n \geq 3$).

Degradation assay. The freeze-dried NP/SA scaffolds (with the mass recorded as W_5) were placed in PBS solution at $37^\circ C$ to assess their degradation performance. The degradation experiment was conducted throughout in a shaker at a speed of 120 rpm. After 1, 3, 5, 7, 10, 14, 21, and 28 d, the PBS buffer was discarded. The scaffolds were then freeze-dried and weighed to

obtain the mass (W_6) of the remaining scaffolds after degradation ($n \geq 3$). The degradation rate was calculated using the following equation:

$$\text{Degradation rate (\%)} = (W_5 - W_6)/W_5 \times 100.$$

Where W_5 represents the initial mass of the freeze-dried scaffolds and W_6 represents the remaining mass of the scaffolds after degradation.

Mechanical property test. The cylindrical samples (with a diameter of 9 mm and a height of 10 mm) were subjected to the compression test on a universal material testing machine (AGS-X 5 KN, Shimadzu, Japan). Testing was carried out at a strain rate of 2 mm min^{-1} at room temperature until the compression ratio was 80%; the maximum load of the experiment was 100 N. The mechanical property test followed the GB/T 7314-2005 standard. The compression modulus and compression strength were calculated based on the stress-strain curve ($n \geq 3$).

PRF preparation. A New Zealand rabbit was anesthetized with the physiological saline solution containing 5% ethyl aminobenzoate. Once the anesthesia took effect, blood was collected from the heart of the New Zealand rabbit. The surgical experiments strictly abided by the Guidelines of the China Health and Family Planning Commission. The preparation process of PRF was performed in accordance with the Guidelines for Care and Use of Laboratory Animals of Lanzhou University and approved by the Animal Ethics Committee of the School of Stomatology, Lanzhou University (LZUKQ-2023-038). The col-

lected blood was stored in a 5 mL glass centrifuge tube without an anticoagulant and immediately centrifuged at 3500 rpm for 12 min. Three layers formed in the tube: the upper layer contained acellular plasma, the bottom layer contained red blood cells, and the PRF was formed within the middle layer (Fig. S2A†).²⁸ The freshly prepared PRF was fixed with 5% formaldehyde, and the fiber structure and main components of PRF were observed by H&E staining and immunohistochemistry. At the same time, through the characterization of the microstructure, porosity, degradation performance and mechanical properties of the above materials, we selected the appropriate proportion of NP/SA (1 : 1) scaffolds. The PRF was extruded into the film using a sterile gauze, which was cut into a small square of $0.5 \text{ cm} \times 0.5 \text{ cm}$. The PRF film loaded onto NP/SA (1 : 1) scaffolds was used for subsequent experiments *in vitro/in vivo*. A summary schematic for scaffold preparation and application *in vitro/in vivo* is shown in Fig. 1.

2.3 Biocompatibility and bone regeneration of NP/SA scaffolds *in vitro*

In order to evaluate the biocompatibility and osteogenic capability of the NP/SA scaffolds, rabbit bone mesenchymal stem cells (rBMSCs) and mouse embryonic osteoblast precursor cells (MC3T3-E1) were employed in this experiment. Freshly prepared PRF was used to formulate PRF-conditioned medium for cell culture. The animal samples used in *in vitro* experiments were licensed by the Ethics Committee of the School of

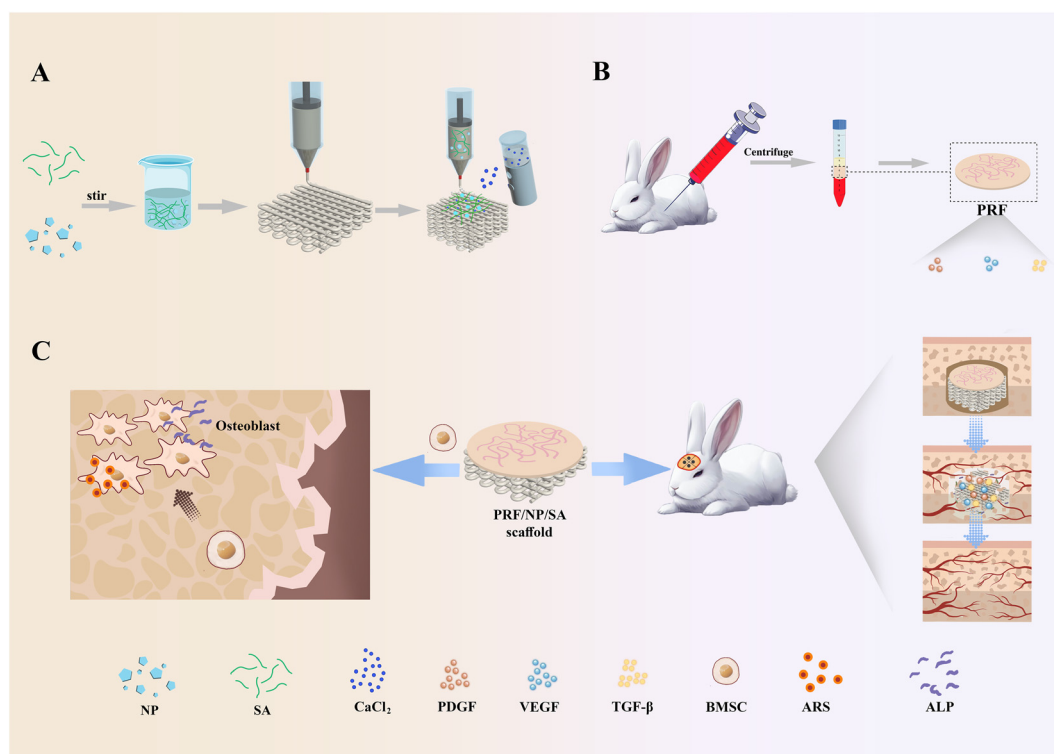


Fig. 1 Schematic illustration of PRF/NP/SA scaffold preparation and application *in vitro/in vivo*. (A) Preparation of NP/SA scaffolds. (B) Preparation process of PRF. (C) Application of PRF/NP/SA scaffold *in vivo* and *in vitro* experiments.

Stomatology, Lanzhou University (LZUKQ-2023-038). Two-week-old rabbits were euthanized by conventional methods to extract and isolate rBMSCs, and passaged to obtain the 3rd to 5th generation of rBMSCs.

2.3.1 Biocompatibility of NP/SA scaffolds

Cell adhesion test. MC3T3-E1 cells were seeded onto scaffolds in 24-plate wells. After one week, the samples were washed twice with PBS and fixed with 2.5% glutaraldehyde at 4 °C for 12 h, then the scaffolds were washed with PBS, and dehydrated with gradient concentrations of ethanol (25%, 50%, 75%, 90%, and 100% for 10 min). Finally, dried scaffolds were observed by SEM to study the morphology of attached cells.

MTT test. The well-grown rBMSCs were cultured separately in high-glucose Dulbecco's modified Eagle's medium (DMEM, PWL037, China) supplemented with 10% fetal bovine serum (FBS, C7074, CellMax, China) and 1% penicillin/streptomycin (MA0110, MEILUNE, China), as well as PRF-conditioned medium. Cells were harvested using trypsin (PWL060, MEILUNE, China) and counted using a hemocytometer (4000, Hausser, U.S.). The SA scaffolds and NP/SA scaffolds were cut into cubes with a diameter of about 5 mm × 5 mm × 3 mm. All scaffolds were disinfected with ethanol (75% v/v) and subsequently sterilized by ultraviolet (UV) light for an additional 30 min on each side. The scaffolds were co-cultured with rBMSCs on 48 well plates with a density of 2×10^4 cells per well for 1, 3, 5, and 7 d, and incubated for 4 h with 100 μ L MTT reagent at 37 °C. The supernatant was discarded, and then DMSO was added to dissolve the purple formazan crystals. The plate was wrapped in foil and placed on an orbital shaker for 15 min to ensure thorough mixing. After that, a 48-well plate was used for detection on a microplate reader (Multiskan FC, Thermo Scientific, U.S.). Absorbance was measured at OD = 490 nm. The data of three parallel experiments were averaged.

Cell viability measurement. The steps of cell culture and the scaffold disinfection were the same as above. The scaffolds were co-cultured with 2×10^4 rBMSCs for 1, 3, 5, and 7 d, the medium was discarded and they were washed twice with PBS (PWL050, MEILUNE, China). The Calcein-AM/PI live-dead cell double staining assay kit was used to stain for 0.5 h. The staining solution was sucked out to terminate the incubation, and an appropriate amount of PBS was added to cover the cells. The living cells (green fluorescence) and dead cells (red fluorescence) were observed under an inverted fluorescence microscope (VERT1, Zeiss, U.S.), and photographed.

2.3.2 Bone regeneration of NP/SA scaffolds *in vitro*

Alkaline phosphatase (ALP) activity. In order to investigate the NP/SA scaffolds' potential in promoting osteogenic differentiation, MC3T3-E1 cells were co-cultured with the scaffolds for 7, 14, and 21 d. After adding cell lysis buffer, the mixture was immediately centrifuged at high speed to collect the supernatant. The centrifugal conditions are 10 000 rpm for 2 min. The supernatant was mixed with the ALP colorimetric reagent (Ritchie Biotech Co., Ltd, China) and detection buffer for 30 min, the reaction was terminated. Finally, the absorbance values of each well were measured using the microplate reader

(Multiskan FC, Thermo Scientific, U.S.) to calculate ALP activity.

Alizarin red staining (ARS). After co-culturing MC3T3-E1 cells with the NP/SA scaffolds for 21 d in the constant temperature incubator, we added 10% formaldehyde solution to each well and fixed them for 10 min. Next, the fixed solution was washed thoroughly with deionized water. Afterward, we added quinizarin red staining solution (provided by Ritchie Biotech Co., Ltd, China) to each well and incubated it for 5 min. The staining solution was washed with deionized water multiple times until the staining solution did not fall off. The samples were observed and photographed using an inverted microscope (VERT1, Zeiss, U.S.).

2.4 Bone regeneration of PRF/NP/SA scaffolds *in vivo*

2.4.1 Calvarial defect model and PRF/NP/SA scaffold implantation. Ten New Zealand rabbits were anesthetized by intravenously injecting 5% ethyl carbamate (5 mL kg⁻¹). The skin was cut and the skull was exposed by blunt dissection. Using a trephine drill, two circular defects with a diameter of 6 mm and a depth of 0.8 mm were prepared on each side of the sagittal suture of the skull. Prior to implantation, each defect underwent thorough sterilization. Subsequently, the defects were implanted with SA, NP/SA, and PRF/NP/SA scaffolds in their respective locations. The surgical experiments strictly abided by the Guidelines of the China Health and Family Planning Commission. All animal procedures were performed in accordance with the Guidelines for Care and Use of Laboratory Animals of Lanzhou University and approved by the Animal Ethics Committee of the School of Stomatology, Lanzhou University (LZUKQ-2023-038). Gentamicin sulfate (Rongrun Biotechnology Co., Ltd, Hebei, China) was intramuscularly injected at 0, 24, and 48 h to prevent postoperative infection after the surgery.

2.4.2 Micro-CT scanning and analysis. The New Zealand rabbits were euthanized at four and eight weeks after surgery to harvest the cranial bone. The harvested cranial bone tissue was fixed by 4% paraformaldehyde solution at room temperature for 24 h. A Hiscan XM Micro-CT (Hiscan Information Technology Co., Ltd, Suzhou, China) was used to take the coronal and 3D reconstructed Micro-CT scanning images to evaluate the new bone formation. Hiscan Analyzer software (Hiscan Information Technology Co., Ltd, Suzhou, China) was used to quantitatively analyse the bone volume fraction (BV/TV) and the bone mineral density (BMD) of the newly formed bone tissue.

2.4.3 Histological and immune-histological assessments. The fixed skull specimens were decalcified in EDTA solution for a duration of 3 months. Subsequently, they were dehydrated through a series of ethanol solutions, ranging from 25% to 100%, and embedded in paraffin. Sectioning (7 μ m thickness) was performed by paraffin slicing microtome (Leica, RM2245, Germany). Tissue sections were stained with Hematoxylin & Eosin (H&E) and Masson Trichrome staining to examine the tissue morphology and new bone formation under the microscope (VERT1, Zeiss, U.S.). To determine

further the potential mechanism of SA, NP/SA, and PRF/NP/SA scaffolds in promoting bone regeneration, we performed immunohistochemical analysis of rabbit skull bone tissue. After deparaffinization and hydration, the sections were blocked with rabbit serum and then incubated with primary antibodies against the osteogenic transcription factor-2 (RUNX-2), vascular endothelial growth factor (VEGF), and type I collagen fibers (COL-1) (diluted 1:100, Abcam). Next, the sections were incubated with enzyme-labelled rabbit anti-mouse secondary antibody (diluted 1:2000, BLOSS). The sections were stained with the 3,3'-diaminobenzidine (DAB) substrate and counterstained with hematoxylin solution. Immunohistochemically stained samples were observed under a light microscope. Additionally, quantitative analysis was performed using NIH ImageJ software (v1.52e) ($n = 3$) based on histological observations.

2.5 Statistical analysis

Statistical analysis of data was performed using ANOVA followed by GraphPad Prism 8 software. Experiments were repeated three times. The results were reported as mean \pm standard deviation and the levels of significance were considered at $*p < 0.05$, $**p < 0.01$, $***p < 0.001$ and $****p < 0.0001$ ($n \geq 3$, n is the number of samples in each group).

3. Results and discussion

3D printing, as an emerging manufacturing technology, has gained significant attention in the field of BTE.²⁹ It boasts various advantages, including personalized design, a suitable specific surface area, and appropriate pore size, distinguishing it from other methods.^{30,31} However, there are few reports on the application of 3D printed NP-based bone materials.^{32,33} One possible reason for the limitation could be attributed to the microscopic lamellar structure of NP (Fig. S1†), which makes it difficult to form a dense micro-network structure with other matrix materials.^{11–13} To overcome this challenge, we incorporated SA as a bio-ink matrix material to enhance the 3D printability and forming ability of NP. SA has been proven effective at forming a dense network structure through Ca^{2+} chemical crosslinking. Additionally, PRF can serve as a growth factor carrier (including BMP, IGF, PDGF, and VEGF) and induce osteogenic differentiation of BMSCs on the surface of the scaffolds.^{34,35} Therefore, leveraging the advantages and physiological characteristics of NP, coupled with the natural biological materials SA and PRF, we fabricated PRF/NP/SA composite scaffolds using 3D printing technology (Fig. 1). The goal was to simulate the trabecular structure of the bone, while exhibiting excellent mechanical properties and osteogenic characteristics.

3.1 Preparation of 3D printed NP/SA scaffolds

The preparation of the printing bio-ink involved mixing SA and NP in specific ratios (NP:SA ratios of 0:1, 1:2, 1:1, and 2:1, w/w). To assess the printability of the bio-ink, rheological

properties were measured. In Fig. S2,† it is observed that with an increasing shear rate, the viscosity of the paste with different NP ratios gradually decreased, demonstrating a clear shear-thinning behaviour. This property plays a crucial role in bio-ink printing because 3D printing requires a certain pressure to reduce the viscosity of the bio-ink as it passes through the nozzle, ensuring smooth extrusion.³⁶ Maintaining an optimal viscosity is crucial because if the viscosity is too high, it can lead to nozzle clogging and difficulties in the printing process. On the other hand, if the viscosity is excessively low, it may cause the hydrogel to collapse, failing to meet the height requirements for printing scaffolds.³⁷ Despite the increase in viscosity with higher NP ratios, this did not affect the overall shear-thinning trend observed in all bio-ink groups. Fig. 2A–D presents the viscoelasticity of the bio-ink in response to shear stress, indirectly reflecting the scaffold's ability to maintain their shape.^{38,39} The shear stress of all four groups printing bio-inks is ≥ 300 Pa. A higher shear stress value indicates better support for maintaining the shape of the bio-ink.³⁶ The storage modulus (G') and loss modulus (G'') respectively represent the energy storage and dissipation during the stress shear process.^{40,41} Upon adding NP to the SA hydrogel, the bio-ink of NP/SA (1:1) exhibited higher G' and G'' values compared to the other three bio-ink groups. This indicates that scaffolds printed with the bio-ink of NP/SA (1:1) should be better able to maintain their structural shape. This finding was consistent with the physical appearance of the printed scaffolds (Fig. 2C), where the NP/SA (1:1) scaffolds exhibited a regular shape and suitable pore size. It is noteworthy that all samples exhibit a higher G'' value than G' , which indicates that the bio-ink does not form a network structure before the Ca^{2+} crosslinking.⁴² The material exhibited viscous deformation, resembling a liquid state,⁴³ which is more suitable for printing. However, the bio-ink was successfully printed as a well-shaped, ordered, and uniformly porous scaffold. This success-

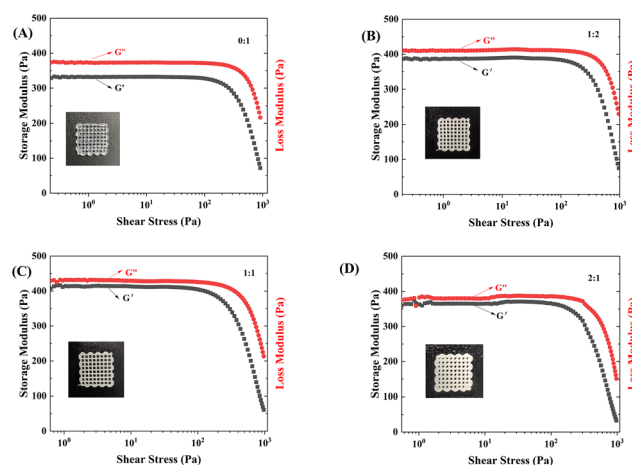


Fig. 2 Rheological behaviours of four groups of printable bio-inks with various NP contents. (A–D) G' and G'' modulus as a function of shear stress for NP/SA (0:1), NP/SA (1:2), NP/SA (1:1) and NP/SA (2:1) bio-ink, respectively.

ful outcome may be attributed to the layer-by-layer electron spray chemical crosslinking of CaCl_2 , preventing the collapse of the scaffold structure.⁴²

3.2 Characterization of NP/SA scaffolds

FTIR spectroscopy is helpful for the characterization of chemical groups of NP/SA composite scaffolds. The FTIR spectrum (Fig. 3A) displayed characteristic peaks of NP at 2515.6, 1791.5, and 866.9 cm^{-1} ,¹² indicating the presence of NP in the scaffold material. The peak at 866.9 cm^{-1} corresponds to the characteristic peak of CaCO_3 , confirming the presence of CaCO_3 in the NP. The peaks at 3453.2 and 1512 cm^{-1} respectively correspond to the stretching vibrations of $-\text{OH}$ and the elongation vibration peak of the $-\text{COO}-$ group.⁴⁴ Upon the addition of NP, the peak associated with the $-\text{COO}-$ group in the NP/SA hydrogel scaffolds shifted to the range of 1562–1580 cm^{-1} . This blue-shift phenomenon could be attributed to the formation of hydrogen bonds between the carbonyl groups of SA and the hydroxyl groups of NP.⁴² Additionally, the intensity of the 866.9 cm^{-1} peak was heightened, corresponding to the bending vibration of the CO_3^{2-} group of NP.^{12,45} The enhancement suggests the successful integration of NP into the NP/SA scaffolds.

The XRD pattern (Fig. 3B) can confirm the presence of CaCO_3 in the scaffolds. The characteristic diffraction peaks of CaCO_3 (JCPDS 41-1475) in the NP are observed at 26.2°, 27.2°, 29.4°, 33.1°, 36.1°, 42.9°, 45.8°, 48.5°, and 52.4°.⁴⁶ The diffraction peaks at 2θ values of 29.4°, 36.1°, 42.9°, and 48.5° correspond to the crystal lattice planes of aragonite calcium carbonate (104), (110), (202), and (116), respectively.⁴⁷ The presence of these peaks indicates the crystal structure of CaCO_3 in the scaffold material, because the main components of NP are CaCO_3 and shell hard protein. In contrast, the XRD spectrum of the pure SA scaffold group does not exhibit distinct characteristic peaks.⁴⁵ As expected, the intensity of the diffraction peaks increases with a higher content of NP in the scaffolds. This suggests that the incorporation of NP enhances the crystallinity of the scaffold material. It is a remarkable fact that CaCO_3 in the NP can undergo complex chemical reactions to transform into hydroxyapatite, a raw material for osteogenesis.⁴⁸ This implies that the NP/SA scaffolds may have the potential to support bone growth and regeneration due to the presence of CaCO_3 and its ability to transform into hydroxyapatite.

Porosity is a crucial indicator for simulating cancellous bone in the scaffolds. In this study, we conducted the porosity

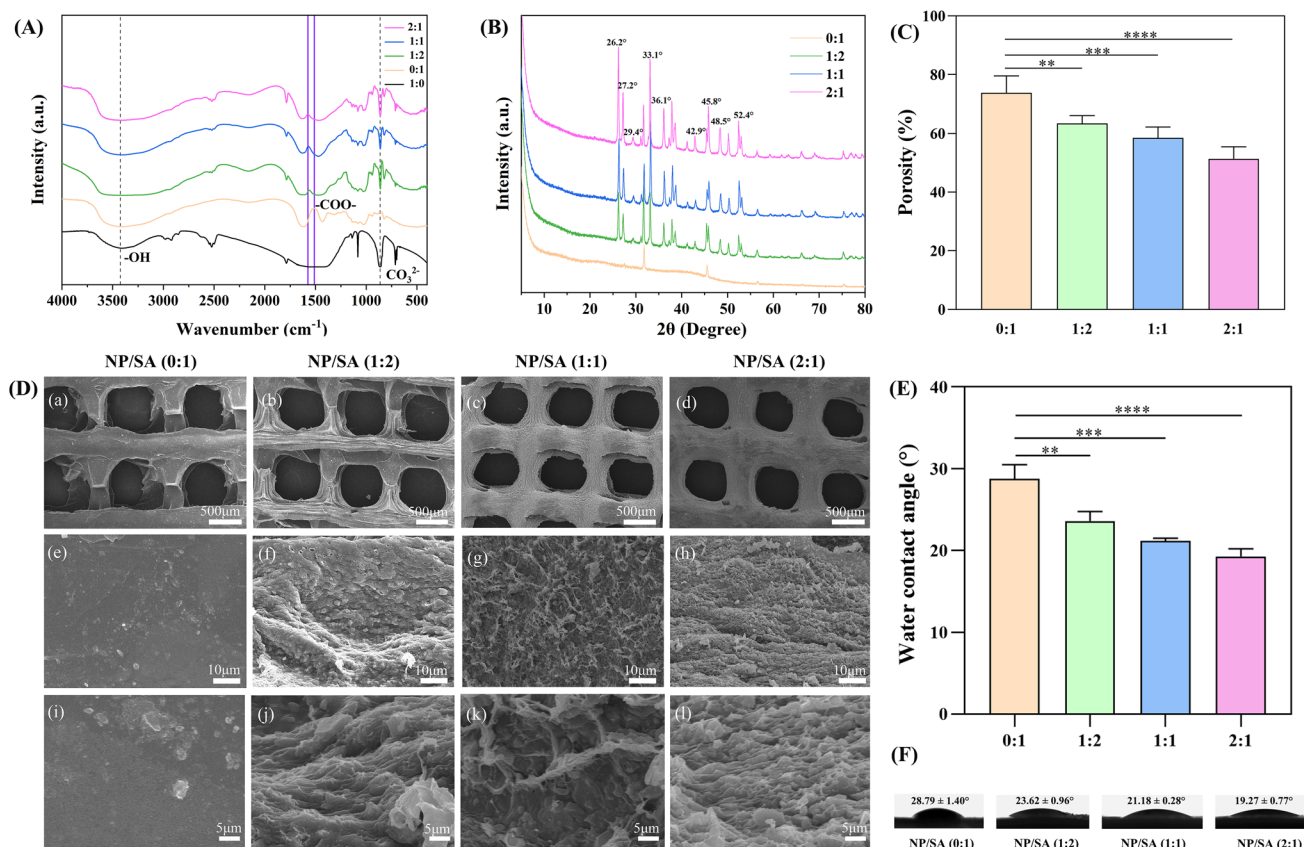


Fig. 3 Physicochemical characterization of NP/SA composite scaffolds. (A) FTIR spectra of NP/SA (0 : 1), NP/SA (1 : 2), NP/SA (1 : 1) and NP/SA (2 : 1) scaffolds. (B) XRD patterns of NP/SA (0 : 1), NP/SA (1 : 2), NP/SA (1 : 1) and NP/SA (2 : 1) scaffolds. (C) Porosity of NP/SA (0 : 1), NP/SA (1 : 2), NP/SA (1 : 1) and NP/SA (2 : 1) scaffolds. (D) SEM images of NP/SA (0 : 1), NP/SA (1 : 2), NP/SA (1 : 1) and NP/SA (2 : 1) scaffolds. (E and F) Water contact angle of NP/SA (0 : 1), NP/SA (1 : 2), NP/SA (1 : 1) and NP/SA (2 : 1) scaffolds. Statistical analysis: * $p < 0.05$, ** $p < 0.01$, *** $p < 0.001$, **** $p < 0.0001$.

test of NP/SA scaffolds by the ethanol displacement method (Fig. 3C). The porosity values for different NP/SA ratios were as follows: NP/SA (0 : 1) – $73.74 \pm 5.81\%$, NP/SA (1 : 2) – $63.38 \pm 2.71\%$, NP/SA (1 : 1) – $58.51 \pm 3.68\%$, NP/SA (2 : 1) – $51.38 \pm 4.06\%$. It is observed that as the NP content increases, the porosity of the scaffolds decreases. This trend can be explained by the fact that a higher content of pearl layer powder, such as NP, may occupy the micropore space structure within the scaffold.⁴⁹ This phenomenon is suggested to be supported by SEM images. The porosity of the NP/SA (0 : 1) group was significantly different from those of the other three groups ($p < 0.01$). Importantly, the porosity of all four scaffold groups exceeded 50%, which met the porosity requirement of cancellous bone trabeculae. The cancellous bone structure is a porous sponge-like structure, and the porosity is mostly 50–90%.⁵⁰ When the porosity of the scaffolds is greater than 50%, it is beneficial for the deposition of the scaffolds bone matrix.⁵¹

The surface morphology of NP/SA composite scaffolds (Fig. 3D) was characterized by SEM. When observed at low magnification (magnification: 35 \times , scale: 500 μm), the scaffolds exhibit relatively large pore sizes, ranging from approximately 400–700 μm . Pore sizes $\geq 300 \mu\text{m}$ are advantageous for the formation of new bone and capillaries because larger pore sizes provide a greater surface area for cell adhesion and proliferation.^{52,53} Under high-magnification observation (magnifications: 1000 and 5000 \times , scales: 10 μm and 5 μm , respectively), the surface of the scaffold material in the pure SA group appeared relatively smooth with uneven crystal materials, which may be caused by the residual CaCl_2 crystallization on the surface of the scaffolds after cross-linking with CaCl_2 .⁵⁴ In contrast, the surfaces of the NP/SA (1 : 2) (Fig. 3Df and j), NP/SA (1 : 1) (Fig. 3Dg and k), and NP/SA (2 : 1) (Fig. 3Dh and l) scaffolds exhibited a sheet-like porous structure with small interconnected pores. The surfaces of these scaffolds also showed a layered “brick-like” microstructure due to the presence of NP.⁵⁵ The microstructure of the scaffold in the NP/SA (1 : 1) group showed a more regular network structure with closer connections, which was beneficial for the transport, metabolism and transportation of nutrients, oxygen and wastes within the scaffolds.^{25,56} Additionally, as the NP content of the scaffolds increased, the pore sizes decreased.⁴⁹ This phenomenon can be attributed to the fact that higher proportions of NP occupy the composite hydrogel space, leading to a reduction in pore size.¹³

Furthermore, water contact angle measurements were performed on the scaffold materials of each group (Fig. 3E and F): the contact angles for the NP/SA (0 : 1), NP/SA (1 : 2), NP/SA (1 : 1), and NP/SA (2 : 1) groups were respectively found to be $28.79 \pm 1.40^\circ$, $23.62 \pm 0.96^\circ$, $21.18 \pm 0.28^\circ$, and $19.27 \pm 0.77^\circ$. Statistical analysis showed significant differences ($p < 0.01$) between the NP/SA (0 : 1) group and the other groups. These results clearly indicate that the addition of NP improves the hydrophilicity of SA. NP is a natural composite material mainly derived from marine shellfish, known for its favourable hydrophilicity.¹¹ Consequently, an increased NP content in the

NP/SA composite scaffolds results in improved hydrophilicity. This improvement in hydrophilicity plays a significant role in promoting cell adhesion and migration.^{12,13}

The high swelling rate of the material often leads to the collapse of the scaffolds and makes the scaffolds lose their original structure.⁵⁷ In addition, high swelling ratio will cause loosening of the bone graft and unfavourable stress on bone tissue and microenvironment around bone graft.⁵⁸ Therefore, we evaluated the swelling ratios for four groups of NP/SA composite scaffolds in the study (Fig. 4A and B). Fig. 4A visually presents the swelling changes observed in the four groups of NP/SA composite scaffolds. The swelling rate of the four groups of scaffolds increased with time within 24 hours. The four groups of scaffolds showed a similar swelling process, but the NP/SA (0 : 1) scaffold group had the highest swelling rate. In 0–2.5 h, the swelling rate increased rapidly, followed by a slow increase. It might be that the four group scaffolds reached the expansion equilibrium and saturated water absorption.⁵⁹ Subsequently, a quantitative analysis of the swelling of the scaffolds was performed (Fig. 4B). The swelling rates of the NP/SA (0 : 1), NP/SA (1 : 2), NP/SA (1 : 1) and NP/SA (2 : 1) scaffolds were determined to be $701.84 \pm 38.2\%$, $526.37 \pm 21.57\%$, $439.39 \pm 14.28\%$, and $361.06\% \pm 5.32\%$, respectively. The results showed that compared with the other three groups, the swelling rate of the NP/SA (2 : 1) scaffold group was lower. The phenomenon may be attributed to the filling of the scaffold network structure with NP, thereby impeding the diffusion of water molecules into the hydrogel.⁶⁰ This suggests that with the increase of NP content, the swelling rate decreases significantly, which is beneficial for the long-term preservation of the scaffolds' microstructure and prevents the collapse of the scaffold.^{24,61} On the other hand, the decrease of swelling rate is more conducive to cell penetration and growth.⁶² The degradation performance of scaffolds is an important factor in tissue regeneration, and the ideal bone scaffolds should have a degradation rate that matches the speed of bone tissue regeneration to facilitate bone regeneration.⁶³ As shown in Fig. 4C, we observed the degradation trend of the NP/SA scaffolds. While the degradation rates of all groups increased with the progression of time, it was observed that the degradation rate slowed down at each time point with an increase in NP content. This showed that the addition of NP regulated the degradation rate of the hydrogel scaffold.⁶⁴ Bone defect repair occurs within four weeks after trauma,^{4,65} so we chose the degradation rate of 4 weeks as an important index to evaluate the degradation performance of NP/SA scaffolds (Fig. 4D). The degradation rates of the NP/SA (0 : 1), NP/SA (1 : 2), NP/SA (1 : 1) and NP/SA (2 : 1) groups were $39.56 \pm 0.79\%$, $25.97 \pm 0.84\%$, $21.94 \pm 0.85\%$ and $31.63\% \pm 0.80\%$, respectively. Compared to the other three scaffold groups, the NP/SA (1 : 1) scaffold exhibited the lowest degradation rate, indicating that the scaffold had the highest preservation rate. The NP/SA (1 : 1) group could better maintain the scaffolds' shape to provide support for cell adhesion.⁶⁶ The NP/SA (1 : 1) scaffold degradation rate had coincided with the observed rate of new bone tissue formation in clinical studies.⁶⁷ Therefore,

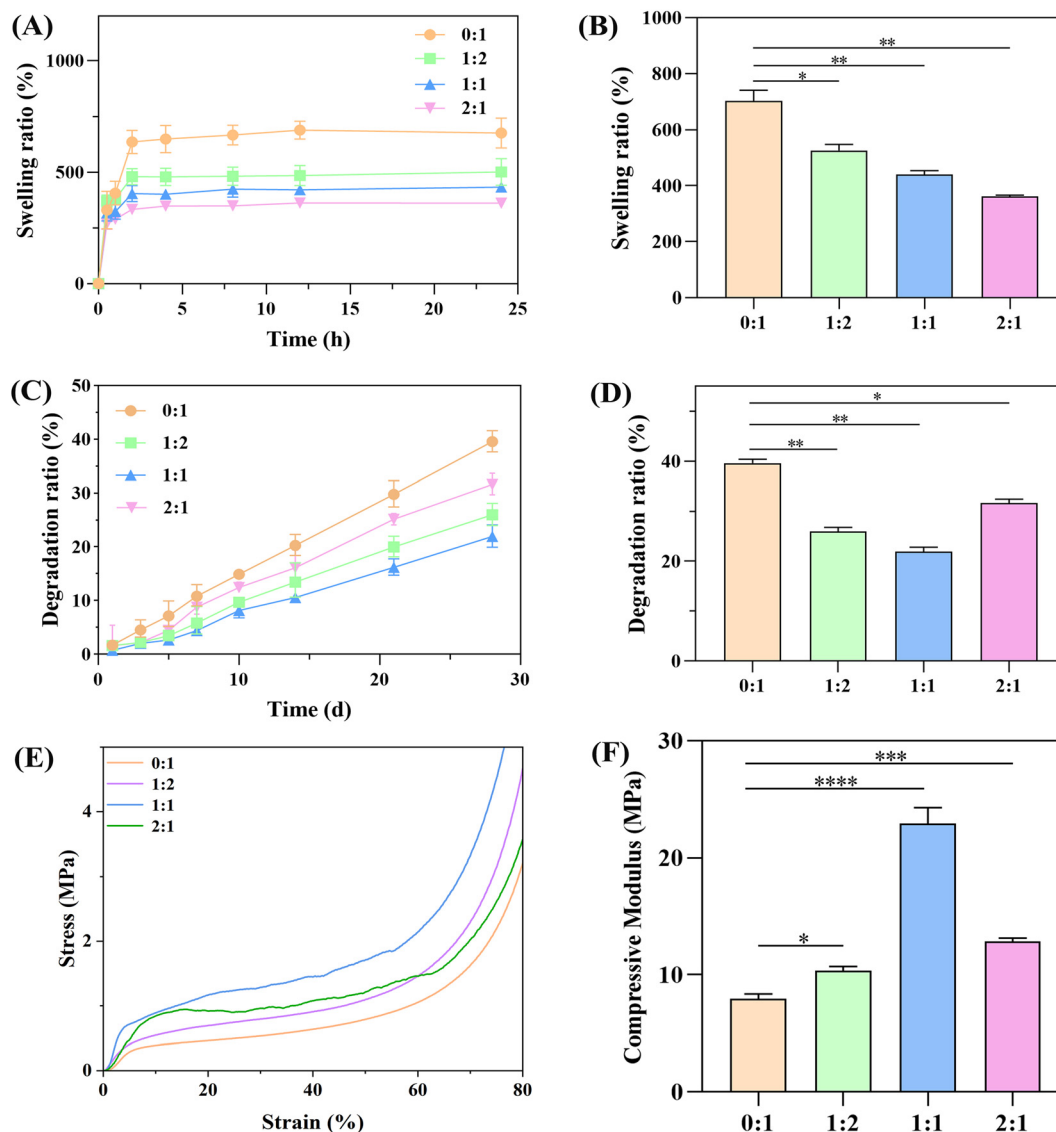


Fig. 4 Physical characterization of various composite scaffolds. (A and B) Swelling behaviours of NP/SA (0 : 1), NP/SA (1 : 2), NP/SA (1 : 1) and NP/SA (2 : 1) scaffolds in water. (C and D) Degradation assay of NP/SA (0 : 1), NP/SA (1 : 2), NP/SA (1 : 1) and NP/SA (2 : 1) scaffolds in PBS at 37 °C. (E) Stress–strain curve of NP/SA (0 : 1), NP/SA (1 : 2), NP/SA (1 : 1) and NP/SA (2 : 1) scaffolds. (F) Compressive modulus of NP/SA (0 : 1), NP/SA (1 : 2), NP/SA (1 : 1) and NP/SA (2 : 1) scaffolds. Statistical analysis: * $p < 0.05$, ** $p < 0.01$, *** $p < 0.001$, **** $p < 0.0001$.

we speculate that the NP/SA (1 : 1) scaffolds may more effectively promote bone tissue regeneration and integration. On the other hand, the NP/SA (2 : 1) scaffolds display an increased degradation rate. This could be attributed to the higher NP content in these scaffolds. As the NP content increases, the relative proportion of SA in the scaffolds decreases.¹⁰ Consequently, NP/SA scaffolds could not form a more compact network structure with the assistance of SA.⁶⁸ Instead, they formed a lamellar structure that may resemble a “shell”.^{13,69} This structural change led to an increase in the degradation rate of the scaffolds.

The compressive performance of NP/SA composite scaffolds was evaluated by analysing stress–strain curves (Fig. 4E) and compressive modulus results (Fig. 4F). The compressive

strengths of NP/SA (0 : 1), NP/SA (1 : 2), NP/SA (1 : 1), and NP/SA (2 : 1) were 7.5 ± 0.60 , 7.55 ± 0.12 , 8.21 ± 0.43 , and 1.27 ± 0.41 MPa, respectively. The compressive modulus of NP/SA (0 : 1), NP/SA (1 : 2), NP/SA (1 : 1), and NP/SA (2 : 1) were 7.97 ± 0.40 , 10.36 ± 0.35 , 22.92 ± 0.84 , and 12.83 ± 0.31 MPa, respectively. The experimental results indicate that the compressive strengths of the NP/SA (0 : 1), NP/SA (1 : 2), and NP/SA (1 : 1) scaffolds all meet the compressive strength of trabecular bone (2–12 MPa).²⁵ However, only the compressive modulus of NP/SA (1 : 1) scaffolds aligns with the mechanical requirements of trabecular bone (0.02–2.94 GPa).⁷⁰ There are significant statistical differences between the four groups. Therefore, the NP/SA (1 : 1) scaffolds may be better suited to fulfill the requirements of trabecular bone, which makes the whole bone matrix

harder. Mechanical properties of the scaffolds with strong osteogenic differentiation potential play a vital role in determining the fate of cells.⁷¹ A harder matrix, which closely matches the characteristics of the bone matrix, is typically considered more suitable for effective bone regeneration.⁴ When the ratio of NP to SA increased to 2:1, the mechanical properties of NP/SA (2:1) decreased. This may be related to the performance of the material itself. We discovered that the material of NP/SA (2:1) scaffolds tends to be more rigid, and the increased brittleness of composite scaffolds leads to the decrease of compressive performance.⁷²

3.3 Verification of PRF

PRF (Fig. S3A†) was prepared by centrifugation of venous blood, and the intermediate layer was PRF. H&E staining and immunohistochemical detection were performed to analyse PRF. H&E staining (Fig. S3B and C†): PRF exhibited three distinct layers when observed under an optical microscope. The red blood cell layer is located at the end of PRF, appearing red without visible nuclear structures. The middle layer was enriched with fibrin, white blood cells, and platelets, exhibiting dense cell aggregation. Some cells were round or oval, and the nucleus was large and round and blue-stained. Additionally, the middle layer contained numerous blue-stained particles without nuclear structures, although their volume was small. The fibrin layer, located on the top of the PRF membrane, shows a sparse red-stained network structure without visible cellular structures. Upon closer examination of the middle layer under a high-power microscope, the aggregation of leukocytes and platelets within the fibrin network was observable. Immunohistochemistry showed that the vascular factors such as PDGF, VEGF, and TGF- β in PRF were at a high expression level (Fig. S3D–F†). The structure and growth factors of PRF are consistent with previous literature reports,²³ the alignment strongly suggests that PRF contains a significant quantity of pro-angiogenic factors, establishing favorable conditions for promoting angiogenesis and facilitating bone formation.

Based on the detection of bio-ink rheological properties, physical characterization, and mechanical performance, we have identified the NP/SA (1:1) ratio as the optimal scaffold group. Subsequently, we loaded PRF onto the NP/SA (1:1) scaffolds and conducted further experiments *in vitro/in vivo*.

3.4 Biocompatibility and bone regeneration of PRF/NP/SA scaffolds *in vitro*

We used rBMSCs as model cells to evaluate the biocompatibility of the scaffolds. In this experiment, rBMSCs were seeded on the surface of pure SA, NP/SA, and PRF/NP/SA scaffolds. MTT assay, cell viability test and SEM were used to detect the proliferation, viability, and adhesion of cells on the scaffold surface. SEM was used to observe the morphology and adhesion of cells on the surface of the scaffolds after 7 d of culture (Fig. S4†). The adhesion ability is a very important aspect in evaluating cell activity.⁷³ Different cells exhibited the expected morphology by adhering to the scaffolds, confirming

that composite scaffolds promoted bone tissue regeneration by simultaneously carrying and supporting rBMSCs.^{74,75} In the SA group and NP/SA group, cells adhere to the surface of the scaffolds and the cell morphology appeared normal, exhibiting an elliptical shape. Compared to the other two groups, the PRF/NP/SA group exhibited that cell differentiation was more mature, and elongated pseudopodia were observed in many cells. This indicates that the introduction of PRF enhances cell adhesion and adaptability. The cell proliferation rate on the scaffolds was assessed by the MTT assay (Fig. 5A). rBMSCs were co-cultured with the pure SA, NP/SA, and PRF/NP/SA scaffolds for 1, 3, 5, and 7 d to observe cell proliferation. The cell viability of all scaffold groups was above 80%, indicating that the composite scaffold was non-toxic and had good biocompatibility, which complied with the ISO10993-5:2009.46 standard.⁷⁶ The absorbance of cell viability gradually increased from day 1 to day 7. Notably, on day 3 and day 5, the number of cells in the PRF/NP/SA scaffold group was slightly lower than the control group but significantly higher than the other two groups. This might be attributed to the release of various growth factors by PRF, which could promote cell proliferation. To further validate the reliability of the MTT assay, Calcein-AM/PI staining was performed. As shown in Fig. 5B, where live cells were stained green, and dead cells were stained red. During the 7 days cultivation period, fewer cells stained with red fluorescence were observed in all scaffold groups, indicating that a large area was occupied by live cells with green fluorescence. This also confirmed the good biocompatibility of the four composite hydrogel scaffolds.

MC3T3-E1 cells were used as seed cells for *in vitro* osteogenic experiments. The biochemical alterations, including heightened ALP activity, increased calcium concentration, and enhanced cell metabolism observed on the surface of scaffolds, serve as indicators of the osteogenic differentiation of BMSCs.^{75,76} In this study, ALP activity and ARS were used to evaluate the osteogenic differentiation potential of pure SA, NP/SA, and PRF/NP/SA scaffolds. The ALP activity of the SA scaffolds, NP/SA scaffolds, and PRF/NP/SA scaffolds on days 7, 14, and 21 of co-culture are depicted in Fig. 5C. The ALP enzyme values for the control group, SA scaffolds, NP/SA scaffolds, and PRF/NP/SA scaffolds after 7 d were 65.08 ± 3.02 , 86.71 ± 2.03 , 103.68 ± 2.01 and $121.19 \pm 1.78 \text{ U L}^{-1}$. By day 21, these values increased to 181.75 ± 2.20 , 189.95 ± 0.52 , 211.62 ± 2.72 , and $249.38 \pm 1.54 \text{ U L}^{-1}$, respectively. ALP activity of PRF/NP/SA scaffolds was significantly higher than that of the other two groups and the control group on days 7, 14, and 21, with a notable difference between the NP/SA group and the PRF/NP/SA group. These results showed that the NP/SA scaffolds exhibited significantly higher ALP activity than the SA scaffolds, suggesting that the inclusion of NP in the scaffolds could enhance the osteogenic activity of MC3T3-E1 cells. This enhancement may be attributed to the main component of NP, aragonite calcium carbonate, which provides essential raw materials for osteogenesis. Moreover, when compared to NP/SA, the PRF/NP/SA group showed significantly increased ALP activity and osteogenic differentiation. This phenomenon may

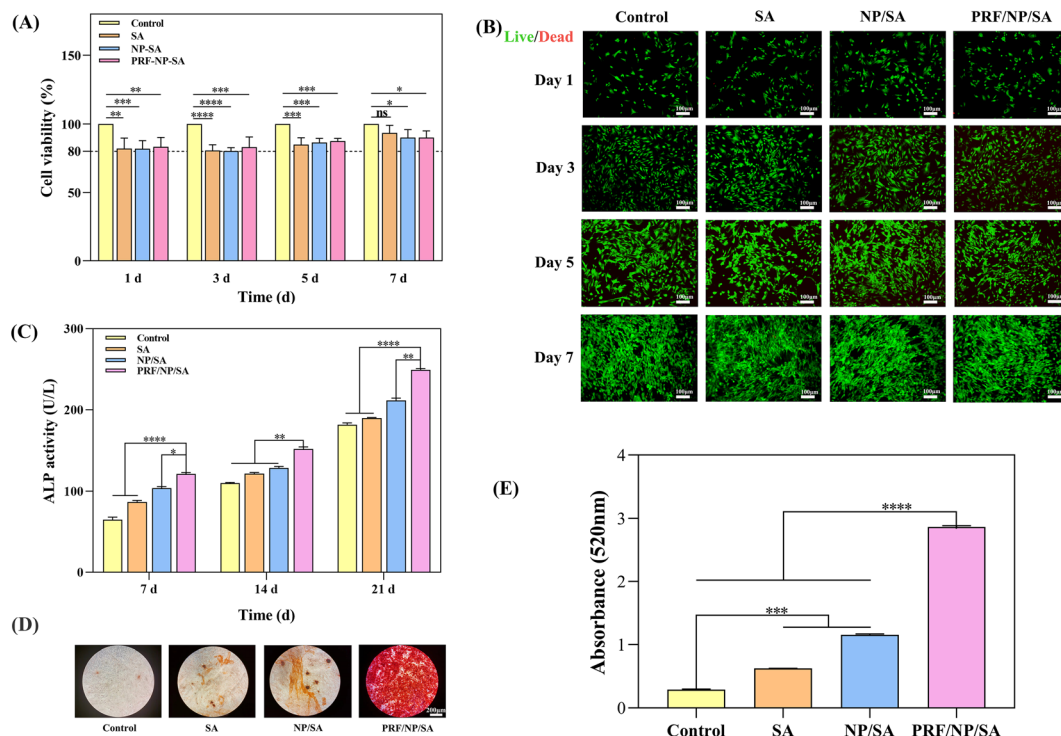


Fig. 5 Biocompatibility and osteogenic activity of different composite scaffolds. (A) MTT test of rBMSCs co-cultured with different composite scaffolds on days 1, 3, 5, and 7. (B) Live and dead staining of rBMSCs co-cultured with different composite scaffolds. (C) ALP activity of MC3T3-E1 cells on SA scaffolds, NP/SA scaffolds, PRF/NP/SA scaffolds, and control group for 7, 14 and 21 d. (D) ARS staining optical microscopy images of scaffolds co-cultured for 21 d. (E) Quantitative analysis of ARS for MC3T3-E1 cells cultured on the surface of scaffolds for 21 d. Statistical analysis: * $p < 0.05$, ** $p < 0.01$, *** $p < 0.001$, **** $p < 0.0001$.

be related to the fact that PRF contains a variety of different growth factors (such as TGF- β , PDGF, IGF, *etc.*), which activate related signalling pathways to promote the induction of the mineralized bone matrix⁷⁷ and further accelerate bone regeneration. ALP plays a crucial role in the initiation of mineralization by facilitating the degradation of organic phosphates and providing sufficient concentrations of inorganic phosphate components (such as Ca and P) for the mineralization process. It serves as an early indicator of osteoblast activity.⁷⁸ ARS is an evaluation technique commonly used to assess the presence of calcium-rich sediments on scaffold surfaces,^{79,80} which allows for the visualization of the osteogenic effect in a straightforward manner. To further assess the mineral deposition of MC3T3-E1 cells after scaffold extract treatment, ARS staining was conducted on the 21st day to evaluate osteogenic effects. Optical microscopy images revealed the presence of mineralized nodules in the culture of the bone induction medium across all groups. However, more mineral matrix formation was observed and quantified in the NP/SA and PRF/NP/SA groups, particularly in the PRF/NP/SA group (Fig. 5D and E). These experimental results also confirmed that scaffolds containing NP and PRF exhibited higher levels of mineral deposition, providing further evidence of the excellent osteogenic performance of NP and the positive influence of PRF on osteogenic differentiation.

3.5 Evaluation of *in situ* bone regeneration

The critical size skull defect model was established in New Zealand rabbits to evaluate the osteogenic effect of pure SA, NP/SA, and PRF/NP/SA scaffolds *in vivo*. Following the establishment of the skull defect model, the corresponding scaffolds were implanted into the corresponding position (Fig. S5†) to reconstruct the surrounding bone structure at 4 W or 8 W. Coronal and three-dimensional reconstruction Micro-CT images were captured at 4 and 8 W after operation to evaluate the effect of bone healing (Fig. 6A). As shown in Fig. 6A, the PRF/NP/SA scaffold group exhibited significantly enhanced new bone formation compared to the other three groups at 4 and 8 W. At 8 W, the new bone volume ratio (BV/TV) of the PRF/NP/SA scaffolds was the highest. Further quantitative analysis of these Micro-CT images also showed similar results. Compared with the SA group, the BV/TV of the PRF/NP/SA group was 3.22 times and the bone mineral density (BMD) was 3.17 times (Fig. 6B and C).

Moreover, we also verified the enhanced bone regeneration performance of pure SA, NP/SA, and PRF/NP/SA scaffolds by H&E and Masson trichrome staining. H&E (Fig. 7A) staining showed that the bone defect area initiated growth from the marginal zone without any discernible signs of inflammatory reaction. After 4 weeks, a modest amount of new bone regeneration was evident in all scaffold groups, accompanied by a sub-

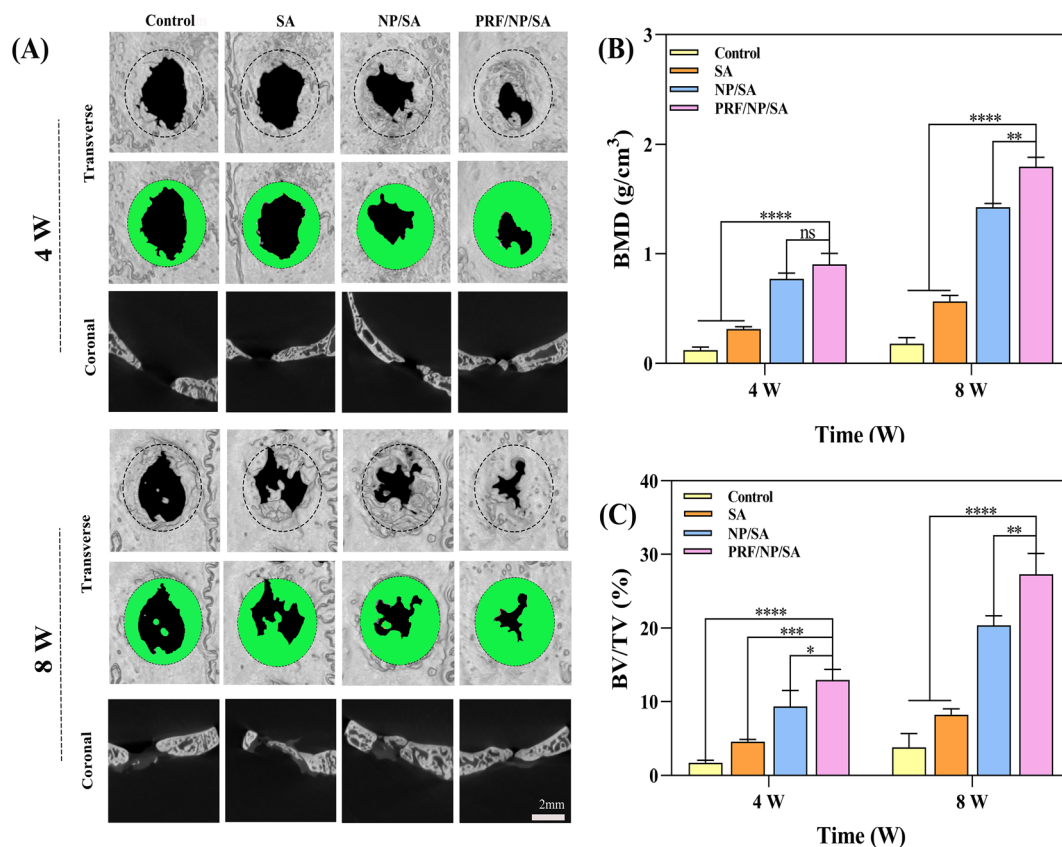


Fig. 6 Bone regeneration of different composite scaffolds *in vivo*. (A) Representative 3D-reconstructed micro-CT images in the defect sites after scaffold implantation for 4 and 8 W (green represents the new bone area in various composite scaffolds). (B) BMD analysis determined by micro-CT at 4 and 8 W. (C) BV/TV analysis determined by micro-CT at 4 and 8 W. Statistical analysis: * $p < 0.05$, ** $p < 0.01$, *** $p < 0.001$, **** $p < 0.0001$.

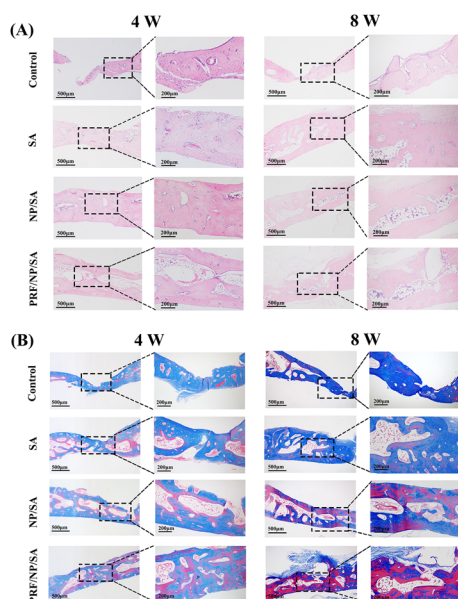


Fig. 7 H&E and Masson staining of skull defect bone regeneration of different composite scaffolds. (A) H&E staining of skull defect bone regeneration of control, SA, NP/SA, and PRF/NP/SA groups at 4 and 8 W. (B) Masson staining of skull defect bone regeneration of control, SA, NP/SA, and PRF/NP/SA groups at 4 and 8 W (the red area represents mineralized bone and the blue area represents collagen fiber protein).

stantial generation of fibrous connective tissue. Histological images indicated a slightly more significant bone formation in the PRF/NP/SA scaffold group. At 8 W, compared to the control group, the defect area of three scaffolds contained less fibrous tissue and displayed visible new bone formation. Magnified histological images indicated significantly higher levels of calcification in the surrounding tissues of the NP/SA and PRF/NP/SA groups when compared to the control and SA groups. Among them, the PRF/NP/SA group displayed the most bone-like structure. To further assess the maturity of newly formed bone, Masson staining was performed (Fig. 7B). The red area represents mineralized bone, and the blue area represents collagen fiber protein; compared to the control group and the SA scaffold group at 4 W, the NP/SA and PRF/NP/SA scaffold groups showed new bone formation (red areas), while non-mineralized collagen stained in blue was detectable in the defect area. The amount of non-mineralized collagen gradually decreased with increasing bone tissue formation, with the control group exhibiting the highest amount of blue-stained collagen. At 8 W post-operation, each group exhibited a dense fibrous tissue layer stained blue and an increased amount of mineralized red-stained bone tissue. In the NP/SA and PRF/NP/SA groups, there was a substantial improvement in newly formed bone tissue and collagen deposition. Moreover, the

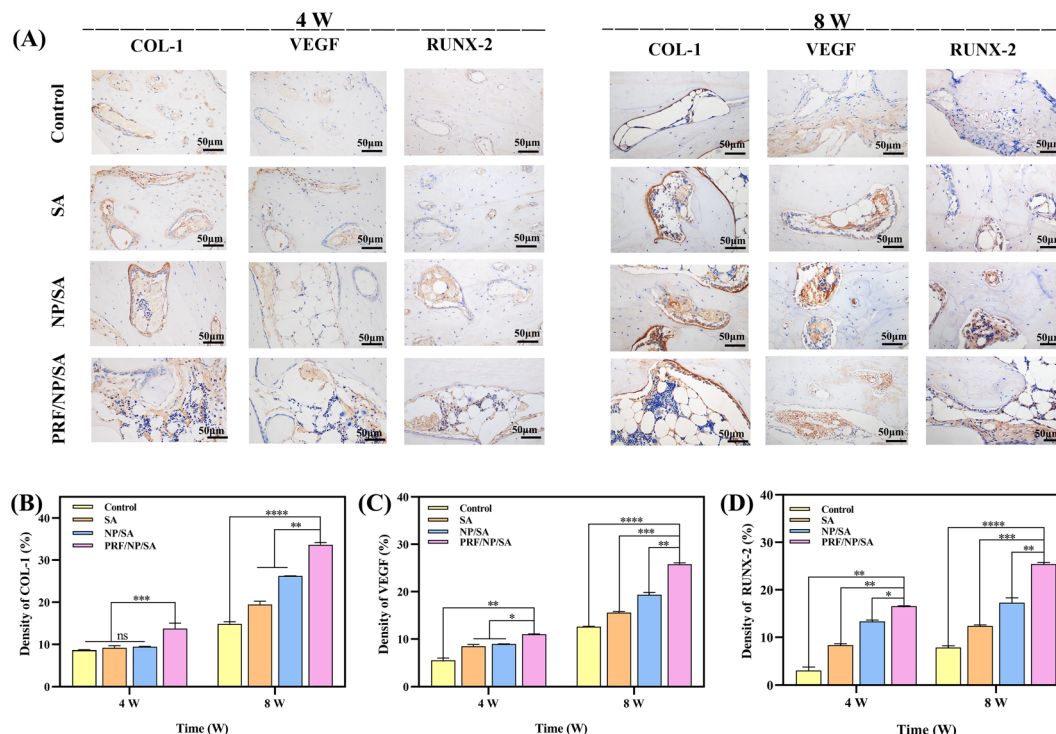


Fig. 8 Immunohistochemistry of skull defect bone regeneration of different composite scaffolds. (A) Immunohistochemistry staining (COL-1, VEGF, and RUNX-2) of skull defect bone regeneration of different composite scaffolds at 4 W and 8 W. (B–D) The quantification of the expression amount of COL-1, VEGF, RUNX-2 at 4 W and 8 W. Statistical analysis: * $p < 0.05$, ** $p < 0.01$, *** $p < 0.001$, **** $p < 0.0001$.

PRF/NP/SA group displayed the presence of trabecular bone structures, indicating its excellent osteogenic properties.

The process of new bone formation coincides with angiogenesis and the proliferation of fibrous connective tissue, closely associated with the expression of relevant proteins.⁷³ In the context of bone development, the transcription factor RUNX-2 plays a pivotal role in osteoblast differentiation, chondrocyte maturation, osteoclast differentiation, and extracellular matrix (ECM) secretion.⁸¹ PRF is enriched with growth factors and cytokines, crucial for cell adhesion and tissue repair. Notably, the vascular endothelial growth factor (VEGF) within PRF stimulates blood vessel formation, enhancing blood supply to damaged tissues and expediting bone formation.⁸² Collagen type I, a well-known component of the bone matrix, is highly expressed during new bone formation.⁸³ Therefore, we explored the expression of related proteins (RUNX-2, COL-1 and VEGF) by immunohistochemical analysis to evaluate osteogenic progression (Fig. 8A). At 4 and 8 W, IHC staining demonstrated higher expression of COL-1, VEGF, and RUNX-2 antibodies in the PRF/NP/SA scaffold group. Subsequently, we performed quantitative immunohistochemical analysis of the above three types of antibodies (Fig. 8B–D). The results were also consistent with the results shown in the immunohistochemical images. This finding shows that the PRF/NP/SA scaffolds possessed favourable osteogenic properties, which may be attributed to the synergistic effect of NP and PRF, ultimately accelerating bone tissue formation.

To sum up, the process of bone repair and regeneration is complex. Tissue engineering scaffolds provide a promising approach to promote osteogenesis. The NP/SA scaffold prepared by 3D printing has a stable structure and good mechanical properties. Effective promotion of new bone formation occurs when the structure and function of the implanted scaffolds align well with natural cancellous bone. The incorporation of PRF, enriched with bioactive substances, notably various vascular growth factors that enhance angiogenesis and expedite bone tissue remodelling, proves highly advantageous in facilitating bone formation. Therefore, the PRF/NP/SA scaffold is very conducive to bone formation and offers a theoretical basis for clinical repair of bone defects.

4. Conclusions

In summary, we have introduced a biomimetic bone scaffold designed to replicate the structure of natural bone trabeculae and exhibit osteogenic properties by integrating 3D printing with the bioactive substance PRF. The NP/SA scaffold leverages the advantages of 3D printing, ensuring appropriate porosity and pore size for cell growth while maintaining satisfactory mechanical properties. Subsequently, PRF was loaded on the above scaffolds. *In vitro* experiments: PRF/NP/SA scaffolds demonstrated the ability to enhance the adhesion and proliferation of rBMSCs, expediting bone tissue regeneration and

repair. Moreover, in a comparative analysis with both the NP/SA scaffold and pure SA scaffold, the PRF/NP/SA scaffold exhibited superior performance in the repair of rabbit cranial defects. Histological and immunohistochemical analyses revealed a high expression level of COL-1, VEGF, and RUNX-2 antibodies in the PRF/NP/SA group. This superiority is attributed to the synergistic effect of PRF and NP, significantly improving the ability of osteogenic differentiation. Our research findings highlight the significant potential of the PRF/NP/SA scaffold for bone regeneration applications. Notably, the PRF/NP/SA scaffold demonstrates high biocompatibility and low immunogenicity. It can be applied in the repair of craniofacial bone and oral alveolar bone regeneration, providing a promising strategy for bone tissue regeneration.

Author contributions

Bin Liu and Cewen Hu: investigation, methodology, formal analysis, and writing – original draft. Xinyue Huang and Kaiqi Qin: methodology, data curation and analysis. Lei Wang and Zhilong Wang: resources and methodology. Jiachen Liang: methodology consultations. Fuqiang Xie: conceptualization, funding acquisition, and writing – review & editing. Zengjie Fan: conceptualization, funding acquisition, supervision, and writing – review & editing.

Conflicts of interest

There are no conflicts to declare.

Acknowledgements

Z. F. thanks the Key Laboratory of Dental Maxillofacial Reconstruction and Biological Intelligence Manufacturing, Gansu Province for providing the experimental platform. Z. F. acknowledges the grants from the National Natural Science Foundation of China (82272500, 81571829), the Natural Science Foundation of Gansu Province (20JR10RA597, 20JR10RA737), the Fundamental Research Funds for the Central Universities (lzujbky-2021-ct08, lzujbkj-2021-kb27), the Innovation-driven Empowerment Engineering Project of Gansu Province (GXH20230817-12), the Lanzhou Science and Technology Plan Project (2023-2-59), the Open Subject Foundation of Key Laboratory of Dental Maxillofacial Reconstruction and Biological Intelligence Manufacturing (20JR10RA653-ZDKF20210101), and the Medical Innovation and Development Project of Lanzhou University.

References

- 1 L. Vidal, C. Kampleitner, M. Á. Brennan, A. Hoornaert and P. Layrolle, *Front. Bioeng. Biotechnol.*, 2020, **8**, 61.
- 2 B. Yuan, S. Zhou and X. Chen, *J. Zhejiang Univ., Sci., B*, 2017, **18**, 303–315.
- 3 S. Verrier, M. Alini, E. Alsberg, S. R. Buchman, D. Kelly, M. W. Laschke, M. D. Menger, W. L. Murphy, J. P. Stegmann, M. Schütz, T. Miclau, M. J. Stoddart and C. Evans, *Eur. Cells Mater.*, 2016, **32**, 87–110.
- 4 L. Zhang, Y. Dong, Y. Xue, J. Shi, X. Zhang, Y. Liu, A. C. Midgley and S. Wang, *ACS Biomater. Sci. Eng.*, 2019, **5**, 6691–6702.
- 5 K. Hochedlinger and R. Jaenisch, *N. Engl. J. Med.*, 2003, **349**, 275–286.
- 6 X. Du, D. Wei, L. Huang, M. Zhu, Y. Zhang and Y. Zhu, *Mater. Sci. Eng., C*, 2019, **103**, 109731.
- 7 Y.-F. Shao, X. Qing, Y. Peng, H. Wang, Z. Shao and K.-Q. Zhang, *Colloids Surf., B*, 2021, **197**, 111401.
- 8 L. Chronopoulou, I. Cacciotti, A. Amalfitano, A. Di Nitto, V. D'Arienzo, G. Nocca and C. Palocci, *Nanotechnology*, 2021, **32**, 095102.
- 9 A. C. Hernández-González, L. Téllez-Jurado and L. M. Rodríguez-Lorenzo, *Carbohydr. Polym.*, 2020, **229**, 115514.
- 10 D. Jain and D. Bar-Shalom, *Drug Dev. Ind. Pharm.*, 2014, **40**, 1576–1584.
- 11 E. M. Gerhard, W. Wang, C. Li, J. Guo, I. T. Ozbolat, K. M. Rahn, A. D. Armstrong, J. Xia, G. Qian and J. Yang, *Acta Biomater.*, 2017, **54**, 21–34.
- 12 A. Flausse, C. Henrionnet, M. Dossot, D. Dumas, S. Hupont, A. Pinzano, D. Mainard, L. Galois, J. Magdalou, E. Lopez, P. Gillet and M. Rousseau, *J. Biomed. Mater. Res., Part A*, 2013, **101**, 3211–3218.
- 13 X. Li, P. Xu, Y. Cheng, W. Zhang, B. Zheng and Q. Wang, *Mater. Sci. Eng., C*, 2020, **111**, 110749.
- 14 D. Duplat, A. Chabadel, M. Gallet, S. Berland, L. Bédouet, M. Rousseau, S. Kamel, C. Milet, P. Jurdic, M. Brazier and E. Lopez, *Biomaterials*, 2007, **28**, 2155–2162.
- 15 Ž. Perić Kačarević, P. Rider, S. Alkildani, S. Retnasingh, M. Pejakić, R. Schnettler, M. Gosau, R. Smeets, O. Jung and M. Barbeck, *Int. J. Artif. Organs*, 2020, **43**, 69–86.
- 16 D. L. Dorcemus, H. S. Kim and S. P. Nukavarapu, *Biomed. Mater.*, 2021, **16**, 035021.
- 17 M. Torsello, A. Salvati, L. Borro, D. Meucci, M. L. Tropiano, F. Cialente, A. Secinaro, A. Del Fattore, C. M. Emiliana, P. Francalanci, G. Battafarano, I. Cacciotti and M. Trozzi, *Int. J. Pediatr. Otorhinolaryngol.*, 2022, **161**, 111253.
- 18 G. Chen and N. Kawazoe, *Adv. Exp. Med. Biol.*, 2018, **1058**, 171–191.
- 19 J. Jiao, Q. Hong, D. Zhang, M. Wang, H. Tang, J. Yang, X. Qu and B. Yue, *Front. Bioeng. Biotechnol.*, 2023, **11**, 1117954.
- 20 Y. Wang, C. Ling, J. Chen, H. Liu, Q. Mo, W. Zhang and Q. Yao, *Biomater. Adv.*, 2022, **140**, 213067.
- 21 C. Feng, W. Zhang, C. Deng, G. Li, J. Chang, Z. Zhang, X. Jiang and C. Wu, *Adv. Sci.*, 2017, **4**, 1700401.
- 22 H. D. Kim, S. Amirthalingam, S. L. Kim, S. S. Lee, J. Rangasamy and N. S. Hwang, *Adv. Healthcare Mater.*, 2017, **6**, 1770120.

- 23 Y.-H. Kang, S. H. Jeon, J.-Y. Park, J.-H. Chung, Y.-H. Choung, H.-W. Choung, E.-S. Kim and P.-H. Choung, *Tissue Eng., Part A*, 2011, **17**, 349–359.
- 24 A. Rastegar, M. Mahmoodi, M. Mirjalili and N. Nasirizadeh, *Carbohydr. Polym.*, 2021, **269**, 118351.
- 25 K. Feigin and B. Shope, *J. Vet. Dent.*, 2019, **36**, 109–123.
- 26 Z. Wang, Y. Weng, S. Lu, C. Zong, J. Qiu, Y. Liu and B. Liu, *J. Biomed. Mater. Res., Part B*, 2015, **103**, 1204–1216.
- 27 J. Kundu, J.-H. Shim, J. Jang, S.-W. Kim and D.-W. Cho, *J. Tissue Eng. Regener. Med.*, 2015, **9**, 1286–1297.
- 28 D. M. Dohan, J. Choukroun, A. Diss, S. L. Dohan, A. J. J. Dohan, J. Mouhyi and B. Gogly, *Oral. Surg., Oral. Med., Oral. Pathol. Oral. Radiol. Endod.*, 2006, **101**, e37–e44.
- 29 E. Di Piazza, E. Pandolfi, I. Cacciotti, A. Del Fattore, A. E. Tozzi, A. Secinaro and L. Borro, *Int. J. Environ. Res. Public Health*, 2021, **18**, 10806.
- 30 X. Zhang and Y. Zhang, *Cell Biochem. Biophys.*, 2015, **72**, 777–782.
- 31 G. Ceccarelli, R. Presta, L. Benedetti, M. G. Cusella De Angelis, S. M. Lupi and R. Rodriguez Y Baena, *Stem Cells Int.*, 2017, **2017**, 4585401.
- 32 X. J. Loh, D. J. Young, H. Guo, L. Tang, Y. Wu, G. Zhang, C. Tang and H. Ruan, *Materials*, 2021, **14**, 2797.
- 33 Q. Huang, S. Xu, Z. Ouyang, Y. Yang and Y. Liu, *Mater. Sci. Eng., C*, 2021, **118**, 111458.
- 34 G. Chernoff, *J. Cosmet. Dermatol.*, 2023, **22**(Suppl 1), 15–27.
- 35 X. Wang, G. Li, J. Guo, L. Yang, Y. Liu, Q. Sun, R. Li and W. Yu, *Exp. Ther. Med.*, 2017, **13**, 1891–1899.
- 36 J. Malda, J. Visser, F. P. Melchels, T. Jüngst, W. E. Hennink, W. J. A. Dhert, J. Groll and D. W. Huttmacher, *Adv. Mater.*, 2013, **25**, 5011–5028.
- 37 S. Das, F. Pati, Y.-J. Choi, G. Rijal, J.-H. Shim, S. W. Kim, A. R. Ray, D.-W. Cho and S. Ghosh, *Acta Biomater.*, 2015, **11**, 233–246.
- 38 A. Parak, P. Pradeep, L. C. du Toit, P. Kumar, Y. E. Choonara and V. Pillay, *Drug Discovery Today*, 2019, **24**, 198–205.
- 39 W. L. Ng, J. M. Lee, W. Y. Yeong and M. Win Naing, *Biomater. Sci.*, 2017, **5**, 632–647.
- 40 Z. Lei, Q. Wang and P. Wu, *Mater. Horiz.*, 2017, **4**, 694–700.
- 41 S. T. Bendtsen, S. P. Quinnell and M. Wei, *J. Biomed. Mater. Res., Part A*, 2017, **105**, 1457–1468.
- 42 H. Zhang, H. Huang, G. Hao, Y. Zhang, H. Ding, Z. Fan and L. Sun, *Adv. Funct. Mater.*, 2021, **31**, 2006697.
- 43 E. B. Duoss, T. H. Weisgraber, K. Hearon, C. Zhu, W. Small, T. R. Metz, J. J. Vericella, H. D. Barth, J. D. Kuntz, R. S. Maxwell, C. M. Spadaccini and T. S. Wilson, *Adv. Funct. Mater.*, 2014, **24**, 4905–4913.
- 44 J. Liang, H. Zeng, L. Qiao, H. Jiang, Q. Ye, Z. Wang, B. Liu and Z. Fan, *ACS Appl. Mater. Interfaces*, 2022, **14**, 30507–30522.
- 45 M. U. A. Khan, S. I. A. Razak, S. Rehman, A. Hasan, S. Qureshi and G. M. Stojanović, *Int. J. Biol. Macromol.*, 2022, **222**, 462–472.
- 46 Y. Liu, Q. Huang and Q. Feng, *Biomed. Mater.*, 2013, **8**, 065001.
- 47 M. M. H. Al Omari, I. S. Rashid, N. A. Qinna, A. M. Jaber and A. A. Badwan, *Profiles Drug Subst., Excipients, Relat. Methodol.*, 2016, **41**, 31–132.
- 48 Y. Shen, J. Zhu, H. Zhang and F. Zhao, *Biomaterials*, 2006, **27**, 281–287.
- 49 X. Gui, B. Zhang, Z. Su, Z. Zhou, Z. Dong, P. Feng, C. Fan, M. Liu, Q. Kong, C. Zhou, Y. Fan and X. Zhang, *MedComm – Biomater. Appl.*, 2023, **2**, e41.
- 50 M. Domingos, F. Intranuovo, T. Russo, R. De Santis, A. Gloria, L. Ambrosio, J. Ciurana and P. Bartolo, *Biofabrication*, 2013, **5**, 045004.
- 51 S. M. M. Roosa, J. M. Kempainen, E. N. Moffitt, P. H. Krebsbach and S. J. Hollister, *J. Biomed. Mater. Res., Part A*, 2010, **92**, 359–368.
- 52 L.-B. Mao, H.-L. Gao, H.-B. Yao, L. Liu, H. Cölfen, G. Liu, S.-M. Chen, S.-K. Li, Y.-X. Yan, Y.-Y. Liu and S.-H. Yu, *Science*, 2016, **354**, 107–110.
- 53 G. Bouet, D. Marchat, M. Cruel, L. Malaval and L. Vico, *Tissue Eng., Part B*, 2015, **21**, 133–156.
- 54 X. Hu, Z. Zhang, H. Wu, S. Yang, W. Zhao, L. Che, Y. Wang, J. Cao, K. Li and Z. Qian, *Biomater. Adv.*, 2023, **152**, 213501.
- 55 B. Bisht, A. Hope, A. Mukherjee and M. K. Paul, *Ann. Biomed. Eng.*, 2021, **49**, 1128–1150.
- 56 X. Gui, Z. Peng, P. Song, L. Chen, X. Xu, H. Li, P. Tang, Y. Wang, Z. Su, Q. Kong, Z. Zhang, Z. Li, Y. Cen, C. Zhou, Y. Fan and X. Zhang, *Bio-Des. Manuf.*, 2023, **6**, 451–463.
- 57 N. F. A.-Z. Tuan Mohamood, A. H. Abdul Halim and N. Zainuddin, *Polymers*, 2021, **13**, 4056.
- 58 R. M. Jin, N. Sultana, S. Baba, S. Hamdan and A. F. Ismail, *J. Nanomater.*, 2015, **2015**, 357372.
- 59 D. Kim, S. Kim and S. Jung, *Polymers*, 2021, **13**, 202.
- 60 H. Yao, J. Kang, W. Li, J. Liu, R. Xie, Y. Wang, S. Liu, D.-A. Wang and L. Ren, *Biomed. Mater.*, 2017, **13**, 015012.
- 61 M. D. Giuseppe, N. Law, B. Webb, R. A. Macrae, L. J. Liew, T. B. Sercombe, R. J. Dilley and B. J. Doyle, *J. Mech. Behav. Biomed. Mater.*, 2018, **79**, 150–157.
- 62 C.-C. Yu, J.-J. Chang, Y.-H. Lee, Y.-C. Lin, M.-H. Wu, M.-C. Yang and C.-T. Chien, *Mater. Lett.*, 2013, **93**, 133–136.
- 63 C. Morris, G. M. Kushner and P. S. Tiwana, *Oral Maxillofac. Surg. Clin. North Am.*, 2012, **24**, 351–364.
- 64 U. K. Roopavath, R. Soni, U. Mahanta, A. S. Deshpande and S. N. Rath, *RSC Adv.*, 2019, **9**, 23832–23842.
- 65 S. Frick, in *Green's Skeletal Trauma in Children*, 2015, pp. 1–15.
- 66 Y. Jin, C. Liu, W. Chai, A. Compaan and Y. Huang, *ACS Appl. Mater. Interfaces*, 2017, **9**, 17456–17465.
- 67 M. C. Bottino, V. Thomas, G. Schmidt, Y. K. Vohra, T.-M. G. Chu, M. J. Kowolik and G. M. Janowski, *Dent. Mater.*, 2012, **28**, 703–721.
- 68 D. Zhao, X. Wang, B. Cheng, M. Yin, Z. Hou, X. Li, K. Liu, C. Tie and M. Yin, *ACS Appl. Mater. Interfaces*, 2022, **14**, 21886–21905.
- 69 M. Rousseau, A. Meibom, M. Gèze, X. Bourrat, M. Angellier and E. Lopez, *J. Struct. Biol.*, 2009, **165**, 190–195.
- 70 A. Anandhapadman, A. Venkateswaran, H. Jayaraman and N. Veerabadran Ghone, *Biotechnol. Prog.*, 2022, **38**, e3234.

- 71 L. Wu, X. Pei, B. Zhang, Z. Su, X. Gui, C. Gao, L. Guo, H. Fan, Q. Jiang, L. Zhao, C. Zhou, Y. Fan and X. Zhang, *Chem. Eng. J.*, 2023, **455**, 140699.
- 72 C. Perier-Metz, G. N. Duda and S. Checa, *Biomech. Model. Mechanobiol.*, 2021, **20**, 1723–1731.
- 73 B. Zhang, W. Wang, X. Gui, P. Song, H. Lei, Z. Li, C. Zhou, Y. Fan and X. Zhang, *Appl. Mater. Today*, 2022, **26**, 101346.
- 74 L. Fiocco, S. Li, M. M. Stevens, E. Bernardo and J. R. Jones, *Acta Biomater.*, 2017, **50**, 56–67.
- 75 E. M. Varoni, S. Vijayakumar, E. Canciani, A. Cochis, L. De Nardo, G. Lodi, L. Rimondini and M. Cerruti, *J. Dent. Res.*, 2018, **97**, 303–311.
- 76 A. Sadeghinia, S. Davaran, R. Salehi and Z. Jamalpoor, *Biomed. Pharmacother.*, 2019, **109**, 1924–1931.
- 77 Q. Li, D. A. Reed, L. Min, G. Gopinathan, S. Li, S. J. Dangaria, L. Li, Y. Geng, M.-T. Galang, P. Gajendrareddy, Y. Zhou, X. Luan and T. G. H. Diekwisch, *Int. J. Mol. Sci.*, 2014, **15**, 8509–8525.
- 78 J. Jaroszewicz, J. Idaszek, E. Choinska, K. Szlajak, A. Hyc, A. Osiecka-Iwan, W. Swieszkowski and S. Moskalewski, *Mater. Sci. Eng., C*, 2019, **96**, 319–328.
- 79 C. A. Gregory, W. G. Gunn, A. Peister and D. J. Prockop, *Anal. Biochem.*, 2004, **329**, 77–84.
- 80 L. Macri-Pellizzeri, N. De Melo, I. Ahmed, D. Grant, B. Scammell and V. Sottile, *Tissue Eng., Part C*, 2018, **24**, 171–178.
- 81 Y. Liu, X. Sun, J. Yu, J. Wang, P. Zhai, S. Chen, M. Liu and Y. Zhou, *BioMed Res. Int.*, 2019, **2019**, 3295756.
- 82 A. R. Farmani, M. H. Nekoofar, S. Ebrahimi Barough, M. Azami, N. Rezaei, S. Najafipour and J. Ai, *Platelets*, 2021, **32**, 183–188.
- 83 J.-S. You, S.-G. Kim, J.-S. Oh and J.-S. Kim, *Implant Dent.*, 2019, **28**, 244–255.